

Antichiral edge states in a square lattice

Peng-Yu Guo(郭鹏宇), Wei Li(黎炜), Junhui Hu(胡君辉), and Hai-Xiao Wang(王海啸)
Citation: Chin. Phys. B, 2025, 34 (**10**): 100307. DOI: 10.1088/1674-1056/add90c
http://cpb.iphy.ac.cn; http://iopscience.iop.org/cpb

What follows is a list of articles you may be interested in

Topological states constructed by two different trivial quantum wires

Jing-Run Lin(林景润), Linxi Lv(吕林喜), and Zheng-Wei Zuo(左正伟)
Chin. Phys. B, 2025, 34 (**1**): 010306. DOI: 10.1088/1674-1056/ad8fa3

Phase diagram and quench dynamics of a periodically driven Haldane model

Minxuan Ren(任民烜), Han Yang(杨焓), and Mingyuan Sun(孙明远)
Chin. Phys. B, 2024, 33 (**9**): 090309. DOI: 10.1088/1674-1056/ad4eb3

High-fidelity topological quantum state transfersin a cavity-magnon system

Xi-Xi Bao(包茜茜), Gang-Feng Guo(郭刚峰), Xu Yang(杨煦), and Lei Tan(谭磊)
Chin. Phys. B, 2023, 32 (**8**): 080301. DOI: 10.1088/1674-1056/acc3f6

Change-over switch for quantum states transfer with topological channels in a circuit-QED lattice

Liu-Yong Cheng(程留永), Li-Na Zheng(郑黎娜), Ruixiang Wu(吴瑞祥), Hong-Fu Wang(王洪福), and Shou Zhang(张寿)
Chin. Phys. B, 2022, 31 (**2**): 020305. DOI: 10.1088/1674-1056/ac2f2e

Topology of a parity-time symmetric non-Hermitian rhombic lattice

Shumai Zhang(张舒迈), Liang Jin(金亮), and Zhi Song(宋智)
Chin. Phys. B, 2022, 31 (**1**): 010312. DOI: 10.1088/1674-1056/ac364a

---

Antichiral edge states in a square lattice

Peng-Yu Guo(郭鹏宇)[1], Wei Li(黎炜)[1], Junhui Hu(胡君辉)[1], and Hai-Xiao Wang(王海啸)[1,2,†]

[1] *School of Physical Science and Technology, Guangxi Normal University, Guilin* 541004, *China*
[2] *School of Physical Science and Technology, Ningbo University, Ningbo* 315211, *China*

(Received 19 April 2025; revised manuscript received 13 May 2025; accepted manuscript online 15 May 2025)

Recent advances in topological phases with broken time-reversal symmetry unveil a novel gapless topological phase, i.e., antichiral edge state, featuring co-propagating along the parallel edges. However, to date, such antichiral edge states are only realized in the modified Haldane model, which are based on the honeycomb lattice. Here, we realize the antichiral edge states in a square-lattice tight-binding model with complex nearest-neighbor coupling and both positive and negative next-nearest-neighbor couplings. In contrast to previous proposals, the complex nearest-neighbor coupling breaks the time-reversal symmetry, and the negative next nearest-neighbor coupling shift two Dirac points in energy. We also propose a possible scheme to realize our model with the assistance of acoustic metamaterials. The existence of antichiral edge states is revealed through full-wave simulation of the band structure and acoustic fields excited by a point source.

Keywords: Haldane model, edge states, acoustic metamaterials

PACS: 03.65.Vf, 05.30.Rt, 43.35.+d

DOI: 10.1088/1674-1056/add90c **CSTR:** 32038.14.CPB.add90c

1. Introduction

The interplay between topology and physics has revolutionized the classification of the phase of matter. A concrete example is the celebrated bulk–edge correspondence in the quantum Hall effect, which unveils the intrinsic connection between the quantized Hall conductance in two-dimensional (2D) electron gas and the topology of the wavefunction. In 1988, Haldane proposed a toy model based on the honeycomb lattice realizing quantized Hall conductance without an external magnetic field,[1] which paves the way to realize the quantum Hall effect in periodic lattice systems. As a hallmark of the quantum Hall insulator, two topologically protected edge states propagate in opposite directions at the two parallel boundaries and are robust against perturbations and defects, which are highly desirable in the application of wave transportation. Later on, tremendous efforts have been devoted to the realization of the Haldane model in various physics systems, including photonic,[2–4] acoustic,[5–9] mechanical,[10–12] and cold atomic systems.[13]

Very recently, an exotic topological state called antichiral edge states was proposed by Colomés *et al.* in a modified Haldane model, where the next-nearest-neighbor hopping term was introduced to act equally in both sublattices.[14] Under this modification, the next-nearest-neighbor hopping will shift the two Dirac points in energy rather than open a bandgap, leading to the formation of dispersive antichiral edge states connecting the projections of two Dirac points. In sharp contrast to the counter-propagation feature of the chiral edge states in the Haldane model, the antichiral edge states propagate in the same directions on both edges when the sample geometry is that of a rectangular strip. Guided by the modified Haldane model, antichiral edge states were first realized in a gyromagnetic photonic crystal by applying opposite magnetic fields on different sublattice sites.[15] Subsequently, antichiral edge states have been proposed and realized in photonic crystals,[16–24] acoustic metamaterials,[25–27] and electric circuits[28] owing to their macroscopic scale and the flexibility in fabrication. From the application perspective, the antichiral edge states open up new opportunities for topological physics and functional devices, e.g., unidirectional bulk transportation,[23] wave splitting beamer.[23,27]

However, to date, the realizations of antichiral edge states in all existing work are based on honeycomb lattice, and it is highly desirable to implement antichiral edge states in other lattice types and explore the possibility of different types of the antichiral edge states. Compared to honeycomb lattice, the square-lattice and the corresponding Brillouin zone has a simpler geometry than that of honeycomb lattice, which may easier for experimental realization. In this study, we propose a square-lattice tight-binding model supporting antichiral edge states, in which the synthetic gauge field is induced by the complex nearest-neighbor coupling. In contrast to previous proposals, the offset between two Dirac points is introduced by the coexistence of positive and negative next nearest-neighbor couplings. We also propose a possible scheme to realize antichiral edge states in our square-lattice tight-binding model with the assistance of acoustic metamaterials. By introducing chiral interlayer coupling, it is possible to generate synthetic

[†]Corresponding author. E-mail: wanghaixiao@nbu.edu.cn

© 2025 Chinese Physical Society and IOP Publishing Ltd. All rights, including for text and data mining, AI training, and similar technologies, are reserved.

gauge field and breaks the time-reversal symmetry in the reduced 2D lattice, which paves a way to achieve antichiral edge states. The full-wave simulation of the band structure and acoustic fields further verify the existence of antichiral edge states.

2. Model and Hamiltonian

We consider a square lattice featured with checkerboard patterned staggered flux.[29] As shown in Fig. 1(a), each unit cell consists of two lattice sites, namely, A-type sites indicated by green dots and B-type sites indicated by orange dots. The distance between A-type site and its nearest neighbor B-type site is a, and the lattice constant is $\sqrt{2}a$. The primitive lattice vectors are $\boldsymbol{a}_1 = (a,a)$ and $\boldsymbol{a}_2 = (-a,a)$, respectively. The hoppings from the A-type to the nearest B-type sites along the arrow direction are $t_1 \mathrm{e}^{\mathrm{i}\phi}$, as indicated in Fig. 1(a). Obviously, the flux per plaquette is $\Phi = \pm 4\phi$. The nearest-neighbor hoppings along the $\boldsymbol{x}-\boldsymbol{y}$ direction are t_2 (see the red lines), while the nearest-neighbor hoppings along the $\boldsymbol{x}+\boldsymbol{y}$ directions are $-t_2$ (see the blue lines). Therefore, the Hamiltonian of the square-lattice tight-binding model consisting of nearest-neighbor and next-nearest-neighbor hoppings can be written as $H = H_{\mathrm{NN}} + H_{\mathrm{NNN}}$, where

$$\begin{aligned} H_{\mathrm{NN}} &= t_1 \sum_{\langle i,j\rangle} \left[\mathrm{e}^{\mathrm{i}\phi}(a^{\dagger}_{i,j} b_{i+1,j} + a^{\dagger}_{i,j} b_{i-1,j}) \right. \\ &\quad \left. + \mathrm{e}^{-\mathrm{i}\phi}(a^{\dagger}_{i,j} b_{i,j+1} + a^{\dagger}_{i,j} b_{i,j-1}) + \mathrm{h.c.}\right], \qquad (1) \\ H_{\mathrm{NNN}} &= -t_2 \sum_{\langle\langle i,j\rangle\rangle} \left[(a^{\dagger}_{i,j} a_{i+1,j+1} - a^{\dagger}_{i,j} a_{i+1,j-1}) \right. \\ &\quad \left. + (b^{\dagger}_{i,j} b_{i+1,j+1} - b^{\dagger}_{i,j} b_{i+1,j-1}) + \mathrm{h.c.}\right]. \qquad (2) \end{aligned}$$

Note that a (b) and $a^{\dagger}$ $(b^{\dagger})$ are the annihilation and creation operators of the site A (B), respectively, and h.c. refer to hermitian conjugates. By applying Fourier transformation, the corresponding Bloch Hamiltonian $H(\boldsymbol{k})$ for the square-lattice tight-binding is

$$\begin{aligned} H(k_x,k_y) &= d_x\sigma_x + d_y\sigma_y + d_0\sigma_0 \\ &= 2t_1\cos\phi\,[\cos(k_x a) + \cos(k_y a)]\,\sigma_x \\ &\quad + 2t_1\sin\phi\,[\cos(k_x a) - \cos(k_y a)]\,\sigma_y \\ &\quad + 4t_2\sin(k_x a)\sin(k_y a)\sigma_0, \qquad (3) \end{aligned}$$

where σ_i $(i = x,y)$ and σ_0 refer to the Pauli matrix and unitary matrix, respectively. Evidently, the effective time-reversal symmetry is broken owing to the nearest-neighbor hopping with phase ϕ, in contrast to the Haldane model that induced by the next-nearest neighbor hopping. It is noted that the periodicity of ϕ is π, and the band structures of $-\pi/2 < \phi < 0$ and $0 < \phi < \pi/2$ are the same. Hereafter we focus on $0 < \phi < \pi/2$ for further investigations.

We then implement the eigen calculation of the tight-binding model by assuming hopping amplitude $t_1 = 1$ and $\phi = \pi/4$ with both the absence ($t_2 = 0$) and present ($t_2 = 0.1$) of the next nearest-neighbor hopping. The band structures are depicted in Fig. 1(b). It is seen that a pair of Dirac points sharing the same energy emerge at X_1 and X_2 when the next nearest-neighbor coupling is absent (see dashed lines), in agreement with the result in Ref. [30]. Interestingly, these two Dirac points (dubbed as DP1 and DP2) are shifted in energy range when the next nearest-neighbor hopping is presented (see solid lines). According to Ref. [30], the Dirac points in momentum space can be regarded as topological charges, where the topological invariant is the winding number,[31]

$$w = \frac{1}{2\pi}\oint_c \mathrm{d}\boldsymbol{k}\cdot\left[\hat{d}_x\nabla\hat{d}_y - \hat{d}_y\nabla\hat{d}_x\right], \qquad (4)$$

where $\hat{d}_{x,y} = d_{x,y}/|\boldsymbol{d}|$. Numerical calculations of the winding number give $w = -1$ and $w = 1$ at X_1 and X_2 points for $0 < \phi < \pi/2$. In fact, the degenerate points correspond to vortex centers in momentum space with non-zero winding numbers. Intuitively, we display the planar vector field $\boldsymbol{d} = (d_x, d_y)$ in the momentum space in Fig. 1(c). It is seen that the vector field possesses topological defects with nonzero winding numbers, with the vortex cores with winding number $w = 1$ $(w = -1)$ lying at X_2 (X_1), corresponding to the band degenerate points. The topological feature of the planar vector fields indicates the stability of the band degeneracies against any continuous deformations, which we will elaborately discuss in the following.

In similar to the zero-energy edge states connecting two Dirac points with opposite chirality in the graphene, it is predicted that a pair of edge states connecting two Dirac points with opposite chirality emerges in our square-lattice tight-binding model when a zigzag boundary is adopted. To this end, we construct a ribbon-like structure that is finite in the $\boldsymbol{x}+\boldsymbol{y}$ direction and periodic in the $\boldsymbol{x}-\boldsymbol{y}$ direction with good quantum number $k_{\parallel} = \frac{1}{\sqrt{2}}(\boldsymbol{k}_x - \boldsymbol{k}_y)$, and implement an eigen calculation. Note that the Dirac points with the same chirality will meet at the same projected point. As expected, the projected band structures in Fig. 1(d) show that two Dirac points (DP1 and DP2) with opposite chirality are connected by two degenerated dispersive edge states, in contrast to the flat (zero-energy) edge states in graphene with zigzag boundary. The eigenstates with zero energy at the right panel of Fig. 1(d) further identify that the zero energy not only traverses the edge states (marked by blue spheres), but also traverses the bulk state (marked by a gray sphere). Remarkably, these two edge states have the same group velocity, indicating that two edge states on both edges propagate in the same direction, as a signature of antichiral edge states.

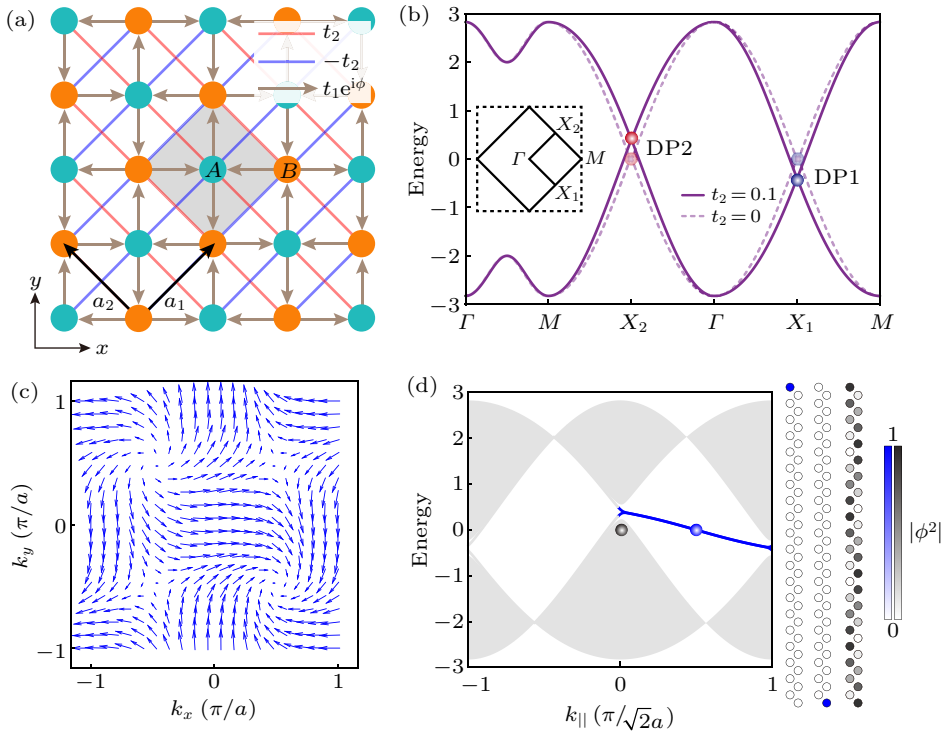


Fig. 1. (a) Schematic diagram of square-lattice tight-binding model supporting antichiral edge states. Green and orange dots represent A and B sites, respectively. (b) The band structure of the square-lattice tight-binding model with $t_1 = 1$, $\phi = \pi/4$ in absence (dashed lines, $t_2 = 0$) and presence (solid lines, $t_2 = 0.1$) of next nearest-neighbor hopping. (c) The distribution of the planar vector field $(\boldsymbol{d}_x, \boldsymbol{d}_y)$, indicating the nonzero winding around X_1 and X_2. (d) The projected band structure of the square-lattice tight-binding model along $k_{\|} = \frac{1}{\sqrt{2}}(\boldsymbol{k}_x - \boldsymbol{k}_y)$. A pair of antichiral edge states are observed.

To unveil the underlying physics of the antichiral edge states in our square-lattice tight-binding model, we investigate the next-nearest neighbor hopping on the shifting of the two Dirac points. For convenience, we defined the energy of DP1 and DP2 as E_1 and E_2 respectively. The offset between DP1 and DP2 is given by $E_{\text{off}} = E_1 - E_2 = 8t_2$ by analytically diagonalizing the Hamiltonian in Eq. (3). Obviously, the energy offset between two Dirac points and the group velocity of the antichiral edge states are depended on the strength of next-nearest neigbhor hopping. In Fig. 2, we plot the evolution of two Dirac points versus the next nearest-neighbor hopping. It is seen that DP2 has higher energy than DP1 when $t_2 > 0$, leading to a pair of antichiral edge states with negative group velocity. In contrast, the positive next nearest-neighbor hopping results in a pair of antichiral edge states with negative group velocity.

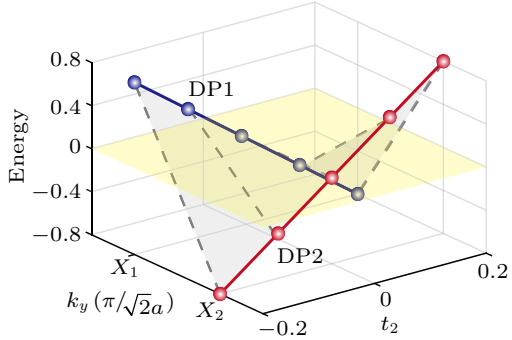


Fig. 2. Evolution of the Dirac points *versus* the next nearest-neighbor coupling. The dashed lines refer to the dispersive antichiral edge states.

3. A possible scheme for experimental realization

In this section, we propose a possible scheme to realize the model by utilizing the acoustic metamaterials. Generally, the breaking of the time-reversal symmetry in an acoustic system is realized with moving background fluids,[5] which drastically increases the engineering complexity. To avoid it, here we follow the general idea about the synthetic gauge field introduced by interlayer coupling in acoustics.[7,30,32] As shown in Fig. 3(a), each coupling tube connects two acoustic resonators at different z coordinates. Note that the coupling between two interlayer acoustic resonators naturally picks up a translation phase $\phi = k_z D$, which generates synthetic gauge field in the reduced 2D lattice [see Fig. 3(b)]. As long as the acoustic structure is periodic in the z direction, the k_z is a good quantum number and the gauge field is preserved when k_z is fixed. On the other hand, to achieve the coexistence of positive and negative next nearest-neighbor couplings, we follow the idea of Ref. [33] by linking acoustic cavities with different connectivity. To be concrete, the straight-linked acoustic resonators has a negative coupling ($\kappa < 0$), while the cross-linked acoustic resonators has a positive coupling ($\kappa > 0$) in our system [see Fig. 3(c)]. We then utilize a commercial finite element software, COMSOL Multiphysics, to calculate the eigenspectra of the acoustic primitive cell. As shown in Fig. 3(d), the Dirac point at X_1 has a frequency than that in X_2, in good agreement with our former theoretical analysis.

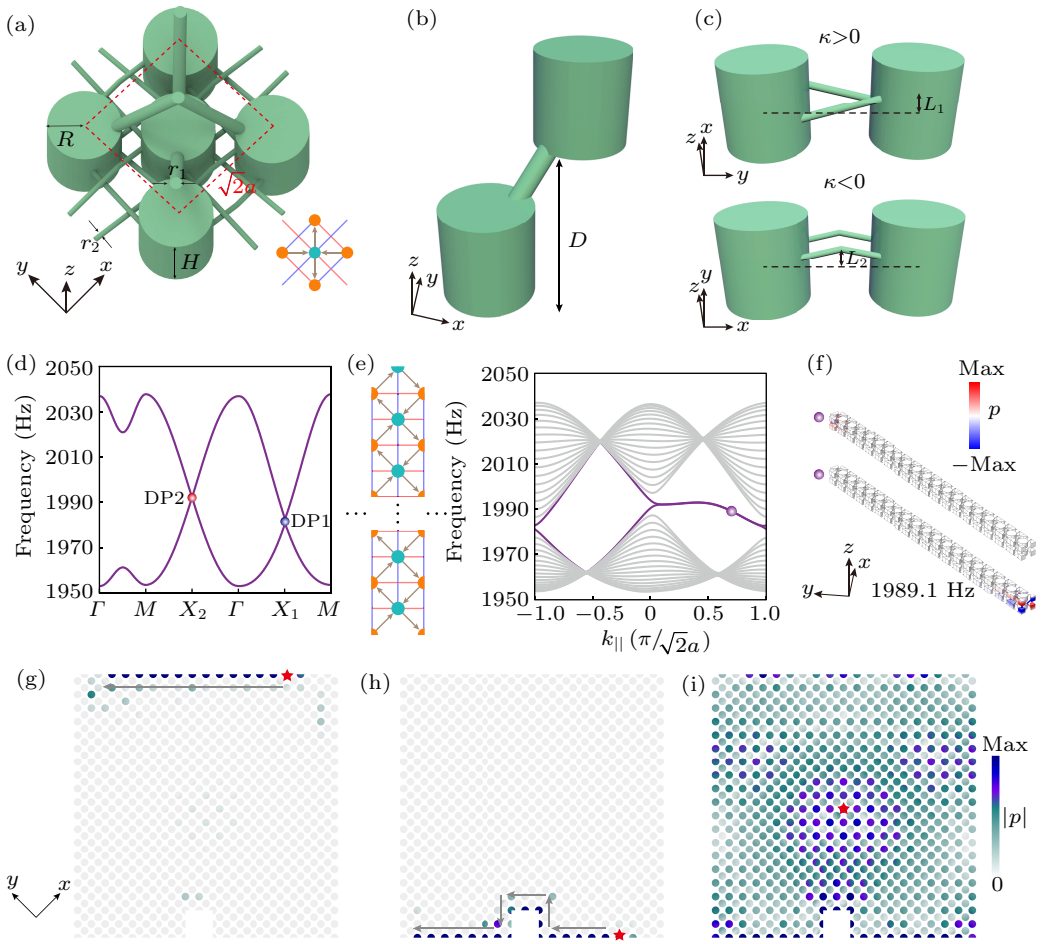


Fig. 3. (a) Acoustic realization of antichiral edge states based on square-lattice tight-binding model, which cylindrical acoustic resonator and connecting tubes are adopted. The geometric parameters are listed as follows: $a = 10$ cm, $R = 0.4a$, $H = 0.85a$, $r_1 = 0.07a$, and $r_2 = 0.03a$. (b)–(c) Schematic diagram of (b) complex coupling between two interlayer resonators with $D = 1.2a$ and (c) positive ($\kappa > 0$) and negative ($\kappa < 0$) couplings between two intralayer resonators. (d) The simulated band structure of the acoustic metamaterials. (e) The simulated projected band structure of ribbon-like acoustic metamaterials consists of 19.5 unit cells. Inset: schematic diagram of the calculated supercell. (f) The acoustic pressure field patterns of the antichiral edge states at a frequency of 1981.1 Hz. (g)–(i) The simulated pressure field pattern of (g) upper and (h) lower antichiral edge states and (i) the excited bulk state at a frequency of 1984 Hz. The red star marks the position of the excited source, the black arrows illustrate the direction of propagation of the sound wave.

To demonstrate the antichiral edge states in our acoustic system, we further construct a ribbon-like acoustic structure that consists of 19.5 unit cells, where the boundary along the $\boldsymbol{x}-\boldsymbol{y}$ ($\boldsymbol{x}+\boldsymbol{y}$) direction is adopted with periodic boundary condition (hard boundary condition). The eigen calculation in Fig. 3(e) shows that two Dirac points in projected band structures are connected by a pair of degenerated edge states, as indicated by the purple lines. Besides, we display the acoustic pressure patterns at a frequency of 1989.1 Hz (marked by purple dots) in Fig. 3(f). It is evident that the acoustic pressures of two modes are mainly localized at opposite edges of the ribbon. In contrast to the linear dispersion with constant group velocity in Fig. 3(d), we notice that the dispersions of the antichiral edge states are dispersive, which mainly attributes to the geometry of the resonator at boundary. To visualize the unique feature of antichiral edge states, we construct a finite acoustic structure with defects, and place the point source at different positions. As shown in Fig. 3(g), an edge state at a frequency of 1984 Hz unidirectionally propagates from right to left along upper boundary when the point source placed at the upper boundary (indicated by the red star) is excited. Owing to the absence of complete band gap, unavoidable bulk modes indicated by the acoustic pressure distribution besides the upper boundary are also observed. When we move the excited point source with the same frequency to the lower boundary, another edge state propagating from right to left and bypassing the defect without being back scattered is excited [see Fig. 3(h)]. Note that the scattering boundary is adopted at left edge of finite acoustic structure in avoiding scattering of bulk states. As a comparison, we also display the acoustic pressure field pattern when the point source is placed at the bulk (see Fig. 3(i)).

To further explore the boundary effect on the dispersion of the acoustic antichiral edge states, we consider three different on-site modulation perturbations. Note that the previous boundaries are formed by incomplete resonators, here we first replace the incomplete resonators of the two edges with complete resonators [see the case-I of Fig. 4(a)]. As shown

in Fig. 4(a), there are two degenerated antichiral edge states at $k_{\|}$ from 0 to 1 in a unit of $\pi/\sqrt{2}a$, indicating that the perturbation does not destroy the antichiral edge band, but only shift it away from the original degeneracy frequency. Furthermore, we design a sector-shaped resonator at boundary (denoted as case-II) to match the linear dispersion of the tight-binding results in Fig. 1(d). The simulated linear dispersion demonstrate that our acoustic antichiral edge states can be effectively tuned by changing the geometric of the end resonators. In Fig. 4(b), we further identify the antichiral edge states under different boundary configurations by presenting the corresponding acoustic pressure field patterns.

Last but not least, we revise the termination of the ribbon-like acoustic structure by setting the number of unit cells as $N = 20$ (denoted as case-III). The eigen spectrum in Fig. 4(c) indicates that there is only a single dispersive edge state band for the case of $N = 20$. The acoustic pressure field patterns in Fig. 4(d) show that one edge state localized at the upper boundary exists in momentum space from -1 to 0, and the other edge states localized at the lower boundary exist in momentum space from 0 to 1. This mode is an even–odd effect due to the chiral symmetry.[34,35] The degeneracy of the edge states at all momentum points including the time-reversal-invariant points is one, which indicates that time-reversal symmetry does not include Kramers degeneracy for bosonic systems.

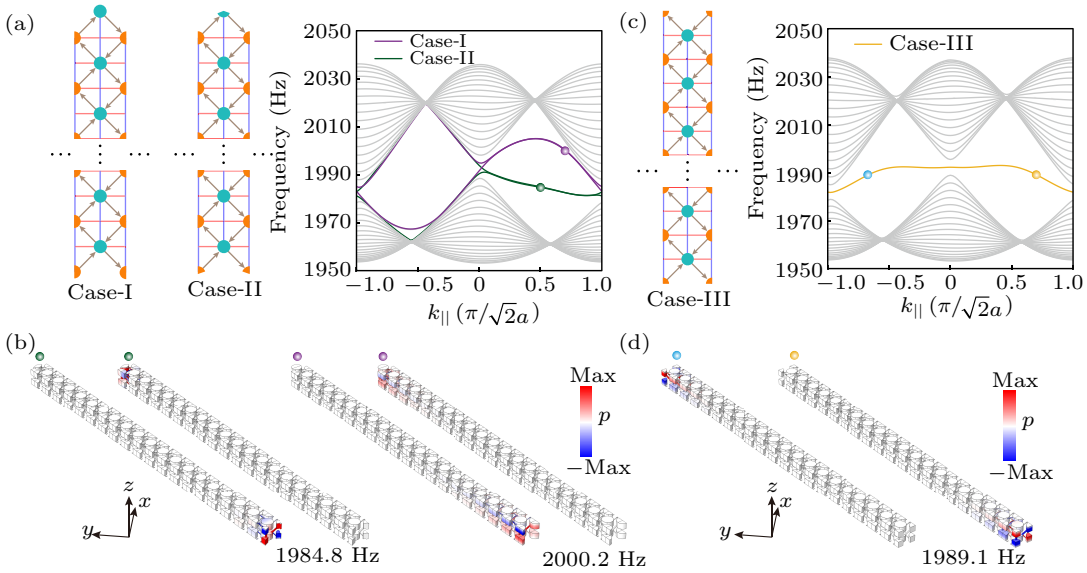


Fig. 4. (a) Left panel: schematic diagram of the edge with complete resonators (denoted as case-I). Middle panel: schematic diagram of the edge with sector-shaped resonators (denoted as case-II). Right panel: the simulated projected band structure of a ribbon-like acoustic metamaterial consists of 19.5 unit cells with different resonators at the edges. (b) The corresponding acoustic pressure field patterns of the antichiral edge states with different boundary configurations. (c) Left panel: schematic diagram of the edge of the corresponding tight-binding model. Right panel: the simulated projected band structure of ribbon-like acoustic metamaterial consists of 20 unit cells with a complete resonator at the edges. (d) The acoustic pressure field patterns of the antichiral edge states at a frequency of 1989.1 Hz.

4. Conclusion

In conclusion, we proposed a square-lattice tight-binding model with complex nearest-neighbor coupling and both positive and negative next-nearest-neighbor couplings, supporting antichiral edge states. In contrast to the modified Haldane model, the time-reversal symmetry breaking is originated from the complex nearest-neighbor coupling, and the negative next nearest-neighbor coupling shifts two Dirac points in energy. As a result, both the energy offset between two Dirac points and the group velocity of the antichiral edge state can be effectively adjusted by tuning the next nearest-neighbor coupling. We also proposed a possible scheme to realize our model with the assistance of acoustic metamaterials. The existence of antichiral edge states is revealed through full-wave simulation of the band structure and acoustic fields excited by a point source.

Acknowledgements

Project supported by the National Natural Science Foundation of China (Grant No. 12474432), the Natural Science Foundation of Guangxi Zhuang Autonomous Region, China (Grant No. 2023GXNSFAA026048), and the Start-up Funding from Ningbo University.

References

[1] Haldane F D M 1988 *Phys. Rev. Lett.* **61** 2015
[2] Haldane F D M and Raghu S 2008 *Phys. Rev. Lett.* **100** 13904
[3] Wang Z, Chong Y D, Joannopoulos J D and Soljačić M 2008 *Phys. Rev. Lett.* **100** 13905
[4] Wang Z, Chong Y, Joannopoulos J D and Soljačić M 2009 *Nature* **461** 772
[5] Yang Z, Gao F, Shi X, Lin X, Gao Z, Chong Y and Zhang B 2015 *Phys. Rev. Lett.* **114** 114301
[6] Khanikaev A B, Fleury R, Mousavi S H and Alù A 2015 *Nat. Commun.* **6** 8260

[7] Xiao M, Chen W J, He W Y and Chan C T 2015 *Nat. Phys.* **11** 920
[8] Ni X, He C, Sun X C, Liu X, Lu M H, Feng L and Chen Y F 2015 *New J. Phys.* **17** 53016
[9] Ding Y, Peng Y, Zhu Y, Fan X, Yang J, Liang B, Zhu X, Wan X and Cheng J 2019 *Phys. Rev. Lett.* **122** 14302
[10] Wang P, Lu L and Bertoldi K 2015 *Phys. Rev. Lett.* **115** 104302
[11] Nash L M, Kleckner D, Read A, Vitelli V, Turner A M and Irvine W T M 2015 *Proc. Natl. Acad. Sci. USA* **112** 14495
[12] Wang Y T, Luan P G and Zhang S 2015 *New J. Phys.* **17** 73031
[13] Jotzu G, Messer M, Desbuquois R, Lebrat M, Uehlinger T, Greif D and Esslinger T 2014 *Nature* **515** 237
[14] Colomés E and Franz M 2018 *Phys. Rev. Lett.* **120** 86603
[15] Zhou P, Liu G G, Yang Y, Hu Y H, Ma S, Xue H, Wang Q, Deng L and Zhang B 2020 *Phys. Rev. Lett.* **125** 263603
[16] Chen J, Liang W and Li Z Y 2020 *Phys. Rev. B* **101** 214102
[17] Wang H, Xie B and Ren W 2023 *Laser & Photon. Rev.* **18** 2300764
[18] Wang J, Ji X, Shi Z, Zhang Y, Li H, Li Y, Deng Y and Xie K 2023 *Eur. Phys. J. Plus* **138** 1149
[19] Wu H, Xu K, Shi Y, Chen P, Poo Y, Liu S and Wu R X 2024 *Appl. Phys. Lett.* **124** 31101
[20] Xi X, Yan B, Yang L, Meng Y, Zhu Z X, Chen J M, Wang Z, Zhou P, Shum P P, Yang Y, Chen H, Mandal S, Liu G G, Zhang B and Gao Z 2023 *Nat. Commun.* **14** 1991
[21] Liu J W, Shi F L, Shen K, Chen X D, Chen K, Chen W J and Dong J W 2023 *Nat. Commun.* **14** 2027
[22] Xie L, Jin L and Song Z 2023 *Sci. Bull.* **68** 255
[23] Chen J and Li Z Y 2022 *Opto-Electron. Sci.* **1** 220001
[24] Chen J and Li Z Y 2022 *Phys. Rev. Lett.* **128** 257401
[25] Yu L, Xue H and Zhang B 2021 *J. Appl. Phys.* **129** 235103
[26] Cheng X, Chen J, Zhang L, Xiao L and Jia S 2021 *Phys. Rev. B* **104** L081401
[27] Wang Y, Liang B and Cheng J 2024 *Phys. Rev. Appl.* **22** 044054
[28] Yang Y, Zhu D, Hang Z and Chong Y 2021 *Sci. China- Phys. Mech. Astron.* **64** 257011
[29] Jiang J H 2012 *Phys. Rev. A* **85** 033640
[30] Yang Z, Gao F, Shi X and Zhang B 2016 *New J. Phys.* **18** 125003
[31] Sun K, Liu W V, Hemmerich A and Das Sarma S 2012 *Nat. Phys.* **8** 67
[32] Wang H X, Lin Z K, Jiang B, Guo G Y and Jiang J H 2020 *Phys. Rev. Lett.* **125** 146401
[33] Qi Y, Qiu C, Xiao M, He H, Ke M and Liu Z 2020 *Phys. Rev. Lett.* **124** 206601
[34] Ryu S and Hatsugai Y 2002 *Phys. Rev. Lett.* **89** 77002
[35] Ma J, Zhou T, Tang M, Li H, Zhang Z, Xi X, Martin M, Baron T, Liu H, Zhang Z, Chen S, Sun X, Ganeshan S, Sun K and Das Sarma S 2025 *Phys. Rev. Lett.* **110** 180403